Front. Earth Sci. 2020, 14(4): 695–710
https://doi.org/10.1007/s11707-020-0819-z

RESEARCH ARTICLE

Regional features of topographic relief over the Loess Plateau, China: evidence from ensemble empirical mode decomposition

Yongjuan LIU[1,3], Jianjun CAO (✉)[2,3,4], Liping WANG[1], Xuan FANG[2,3], Wolfgang WAGNER[4]

1 School of Environment Science and Spatial Informatics, China University of Mining and Technology, Xuzhou 221116, China
2 School of Geography Science/Key Laboratory of Virtual Geographic Environment of Ministry of Education, Nanjing Normal University, Nanjing 210023, China
3 School of Environmental Science, Nanjing Xiaozhuang University, Nanjing 211171, China
4 Department of Geodesy and Geoinformation, Vienna University of Technology, Vienna 1040, Austria

Abstract Landforms with similar surface matter compositions, endogenic and exogenic forces, and development histories tend to exhibit significant degrees of self-similarity in morphology and spatial variation. In loess hill–gully areas, ridges and hills have similar topographic relief characteristics and present nearly periodic variations of similar repeating structures at certain spatial scales, which is termed the topographic relief period (TRP). This is a relatively new concept, which is different from the degree of relief, and describes the fluctuations of the terrain from both horizontal and vertical (cross-section) perspectives, which can be used for in-depth analysis of 2-D topographic relief features. This technique provides a new perspective for understanding the macro characteristics and differentiation patterns of loess landforms. We investigate TRP variation features of different landforms on the Loess Plateau, China, by extracting catchment boundary profiles (CBPs) from 5 m resolution digital elevation model (DEM) data. These profiles were subjected to temporal-frequency analysis using the ensemble empirical mode decomposition (EEMD) method. The results showed that loess landforms are characterized by significant regional topographic relief; the CBP of 14 sample areas exhibited an overall pattern of decreasing TRPs and increasing topographic relief spatial frequencies from south to north. According to the TRPs and topographic relief characteristics, the topographic relief of the Loess Plateau was divided into four types that have obvious regional differences. The findings of this study enrich the theories and methods for digital terrain data analysis of the Loess Plateau. Future study should undertake a more in-depth investigation regarding the complexity of the region and to address the limitations of the EEMD method.

Keywords catchment boundary profile, topographic relief period, ensemble empirical mode decomposition, Loess Plateau

1 Introduction

Landform morphology is the most basic and important geographic parameter. Landforms such as mountains, hills, plains, and basins are the result of complex processes, during which the Earth's surface undergoes changes directed by the effects of endogenic and exogenic forces (MacMillan and Shary, 2009; Wyrick et al., 2014; Tammelin and Kauppila, 2018). The nonuniform spatial distribution of these forces is the root cause behind the formation of various complex landforms. The variation that exists in topographic relief features plays a decisive role in shaping patterns of matter flow and energy conversion on the Earth's surface, and also makes a considerable contribution to constraining the scale and layout of human activities (Black and Perron, 2017; Cowley et al., 2017; Cao et al., 2019).

Landforms that formed under relatively stable conditions of matter, energy, and time tend to exhibit self-similarities (Zhou et al., 2010; Bollati et al., 2017; Yang and Zhou, 2017; Serrano et al., 2018). In particular, rolling landforms (e.g., barchans and undulating folded mountains) tend to exhibit relatively regular spatial wave-like patterns. For such landforms, the mean distance between

Received September 10, 2019; accepted February 14, 2020

E-mail: jjcao@njnu.edu.cn

two adjacent peaks is referred to as the topographic relief period (TRP). In the loess hill-gully areas of the Loess Plateau, rainfall erosion is the major landform-shaping force, which is due to the uniform composition of the Earth's surface in the region and the relative stability of the Ordos platform (Leger, 1990; Bi et al., 2012; Wang et al., 2010; Xiong et al., 2016; Li et al., 2018; Na et al., 2018). Mature loess landforms also exhibit substantial degrees of self-similarity in topographic relief. Thus, it is of theoretical significance to use the TRP to define and quantitatively describe the regular patterns of rolling topographic landforms, especially the distinctive landforms of the Loess Plateau.

In-depth research of topographic relief has been conducted from different perspectives, including the descriptive representation of topographic relief features (Mackay and Band, 1998; Collier et al., 2003; Marston and Jenny, 2015; Orengo and Petrie, 2018), typology of landforms (Gomez, 1984; Orr et al., 2008; de Matos-Machado et al., 2019), the impact on socioeconomic development (Bumbak and Ilies, 2014; Allen, 2009; Telbisz et al., 2014; Zhang et al., 2019), ecological environment evaluation (Wang et al., 2015; Persendt and Gomez, 2016; Savvides et al., 2016), and the relationship with natural disasters (Latrubesse et al., 2009; Iverson et al., 2015). Descriptive representations of topographic relief features have been explored in terms of the extraction method (Xiong et al., 2017; Orengo and Petrie, 2018; Gailleton et al., 2019; Yang et al., 2019), the minimum computational unit (Khan et al., 2016; Meng et al., 2018; Gruber et al., 2019), a suitable representation window (Li, 2015), and prediction modeling (Nunalee et al., 2015; Li et al., 2018). Moreover, combinations of measures — such as relative relief, altitude above sea-level, and topographic waviness — have been used to define the boundaries between China's three terrains, the topology and boundaries of mountainous terrains, the topology of landforms (Clarke and Romero, 2017), and the relationship between topographic waviness and administrative divisions (Robl et al., 2017; Zhang et al., 2017). Furthermore, the impact of topographic relief on economic development, such as population distribution (Liu et al., 2015; Badgley et al., 2017), human settlement distribution (Hui et al., 2015; Xi et al., 2018), and the spatial distribution of poverty (Zhou et al., 2018), has been analyzed at various spatial scales using spatial auto-correlation and coupling methods. Human ecological environments — such as the spatiotemporal distributions of atmospheric pollution (Zhao et al., 2019), the value of ecosystem service (Dymond et al., 2017), soil erosion (Gu et al., 2016; Li et al., 2018), climate change (Karim et al., 2016), land utilization change (Machowski et al., 2016), and farmland productivity — have been evaluated using methods such as the modeling of positive-negative factors and spatial metrics, the topographic gradient effect (Martel, 2016), geographic information system-enabled spatial analysis, topographic heterogeneity (Diefenderfer et al., 2018), sunshine duration (Ambreen et al., 2015), and the topographic control effect. The quantitative relationship between landslide and topographic waviness has also been obtained using rectangular neighborhood analysis window and mean change point analysis methods.

In summary, topographic relief has a significant impact on the human living environment and production activities, and also provides a major measure of landform typology. The most commonly used measure of topographic relief features in the literature is topographic waviness, which is defined as the difference between the altitudes above sea level of the highest and lowest points for a given area. It is a measure for describing regional topographic features at the macro scale, but considers only the vertical dimension of topographic relief, not the horizontal dimension, which can be measured by the TRP.

TRPs reflect the tectonic movements that underlie landform features as well as the overall peripheral structure of regional landforms. This is particularly so on the Loess Plateau, where severe water and soil losses are experienced as a result of runoff erosion; hence, landform features at catchment boundaries reflect pre-erosion topography to a certain degree (Li et al., 2017). Catchment boundaries (i.e., divides) are the highest edge line of a given catchment, and have relatively stable topographic features because they are generally almost immune to runoff erosion (the so called 'erosion-free zone'). Although a catchment boundary profile is not a topographic profile in the general sense, it can be considered to be a spectral line. In contrast to general topographic profiles, vertical catchment boundary profiles are more representative of a catchment's basic topographic features because they i) have a spatially determinate position, ii) are not anisotropic, and iii) reflect the overall topography of a catchment to a certain degree. A preliminary study showed that catchment boundary profiles of similar landforms have similar morphological and structural features at a certain scale.

Catchment boundary profiles are insignificantly affected by topographic anisotropy, statistical error, and the resolution of digital elevation model (DEM) data; hence, they can be used as the basic data for macro topographic characterization owing to their reliability and stability (Farkas et al., 2016). Catchment boundary profiles have spatially determinate positions and reflect the overall morphological characteristics of catchment landforms to a certain degree. In the present study, the catchment boundary profiles of 14 sample areas on the Loess Plateau were obtained from a 5 m resolution DEM dataset. The topographic relief characteristics of various types of landforms on the Loess Plateau were obtained by analyzing the catchment boundary TRP characteristics using the ensemble empirical mode decomposition (EEMD) spectral analysis method. This study aim to demonstrate the effectiveness of spectral analysis for analyzing digital terrain data and the potential of obtaining

different spatial patterns of topographic relief for various landforms on the Loess Plateau.

2 Materials and methods

2.1 Study area

The Loess Plateau extends across a vast area (100°54' E–114°33' E, 33°43' N–41°16' N) that is located to the west of the Taihang Mountains, east of the Riyue-Helan Mountains, north of the Qin Mountains, and south of the Yin Mountains. The 14 sample areas that were selected for this study include Yulin, Jiaxian, Hengshan, Suide, Jingbian, Yan'an, Yichuan, Fuxian, Huanglong, Luochuan, Xunyi, Pucheng, Yongshou, and Qianyang (Table 1). These sample areas are evenly distributed across the northern Shaanxi part of the Loess Plateau and are representative of the wider Loess Plateau.

2.2 Data sources

All data used in this study were extracted from DEMs with a resolution of 5 m. After manual correction, data were obtained for the CBP of the 14 study sites. DEM data were provided by the National Bureau of Surveying and Mapping and Geographic Information and used to generate a 1:10000-scale topographic map at 1 m contour intervals. First, the topographic map was drawn via ground surveys and scanned into a computer for geometric correction. Then, the contour lines were digitized and interpolated into a triangulated irregular network (TIN). Finally, the TIN data that were interpolated from grid digital elevation data were manually edited to correct for errors. Extraction was performed in four steps (Fig. 1): 1) extraction of drainage networks; 2) segmentation of rivers; 3) selection of representative drainage catchments; 4) data export for the selected typical catchment boundaries using commands in the ArcToolbox window. Terrain feature points (e.g., catchment outlet, local peaks, and saddles) were identified from catchment boundary profiles (Fig. 2).

2.3 Methods

Empirical mode decomposition (EMD) is affected by the frequency of the original signal, and thus has the disadvantages of the edge effect and scale mixture. Therefore, Wu et al. (2009) proposed a new data analysis

Table 1 Geographic descrition of the study sites

Sampling sites	Geographic location	Landform types
Yulin	109°32'23"–109°44'7"E 38°38'47"–38°45'28"N	Aeolian and dune
Jiaxian	109°59'33"–110°11'10"E 38°12'45"–38°19'29"N	Loess hill
Hengshan	109° 5'22"–109°16'60"E 37°38'18"–37°44'57"N	Loess hill
Suide	110°3'27"–110°14'58"E 37°27'19"–37°34'3"N	Loess hill
Jingbian	108°32'8"–108°43'44"E 37°11'51"–37°18'26"N	Loess ridge–hill
Yan'an	109°30'46"–109°42'10"E 36°19'16"–36°25'56"N	Loess ridge–hill
Yichuan	110°4'12"–110°15'31"E 36° 5'21"–36°12'4"N	Loess ridge
Fuxian	108°40'8"–108°51'32"E 35°52'13"–35°58'48"N	Loess ridge
Huanglong	109°53'42"–110°4'59"E 35°43'29"–35°50'11"N	Loess ridge–tableland
Luochuan	109°26'37"–109°37'54"E 35°31'17"–35°37'56"N	Loess tableland
Xunyi	108°19'7"–108°30'26"E 35° 1'29"–35°8'3"N	Loess fragmented tableland
Pucheng	109°36'02"–109°47'13"E 34°50'20"–34°57'00"N	Loess fragmented tableland
Yongshou	108°4'20"–108°15'38"E 34°46'5"–34°52'37"N	Loess fragmented tableland
Qianyang	107°4'34"E–107°15'56"E 34°43'55"–34°50'22"N	Loess fragmented tableland

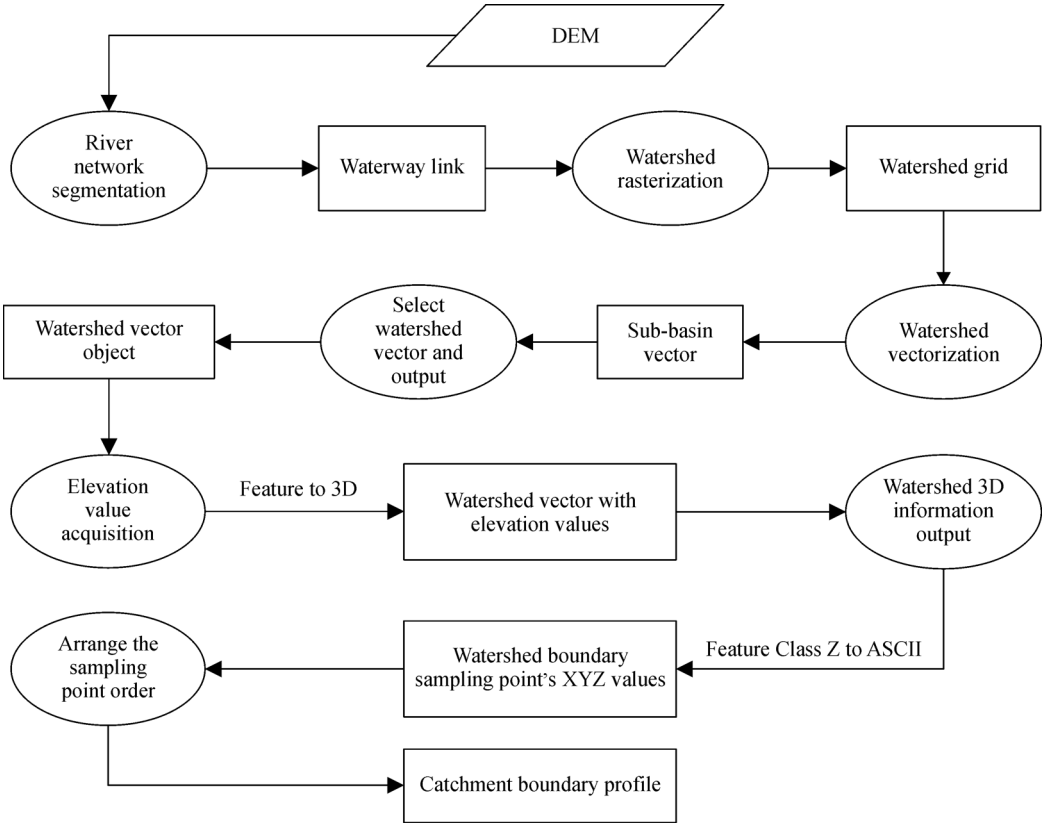

Fig. 1 Process flow for extracting catchment boundary profiles. DEM: digital elevation model.

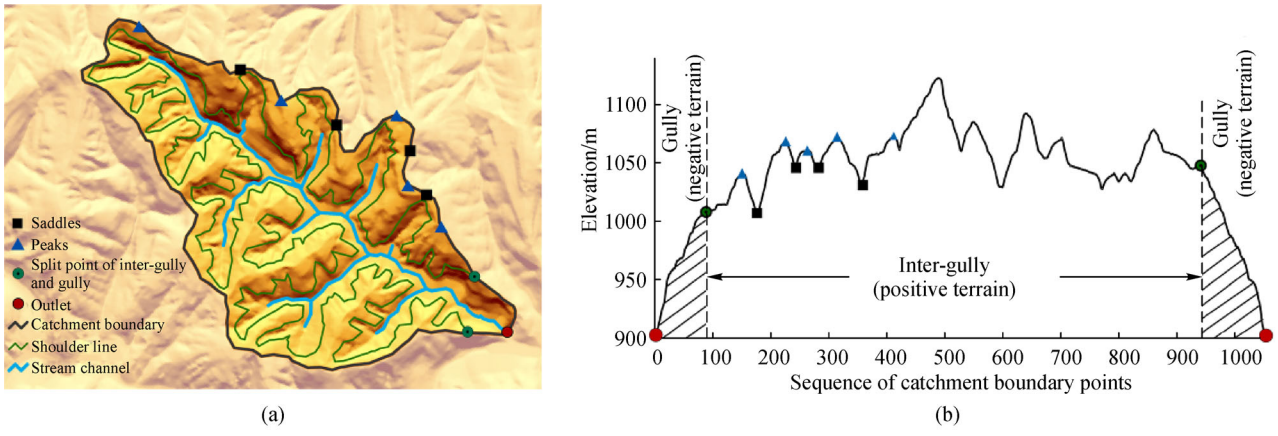

Fig. 2 Morphological parsing of catchment boundary profiles (CBP). (a) Catchment boundary on the surface with shaded relief as background. (b) CBP (unfold with an anticlockwise direction).

method based on EMD: ensemble EMD (EEMD). Compared with EMD, EEMD is a time series analysis method with local self-adaptation; it is essentially a noise-aided data analysis technique that works by adding white noise to a signal to generate a noised-signal ensemble as a new signal, which is decomposed to obtain modally-consistent components of intrinsic mode functions (IMFs). The signal consists of components of different scales that are stacked onto a background with a uniform distribution of white noise in the entire time-frequency space. The signal components automatically distribute themselves to appropriate reference scales. Moreover, owing to the zero-mean-value characteristic of white noise, the added white noise can be averaged out after sufficient trials. Thus, the decomposition result for the noise-added signal can be taken as the result for the original signal, which better reflects the characteristics of the original signal.

In this study, EEMD involved an eight step process:

1) An original signal (a data series), $x(t)$, was stacked onto white noise, $w(t)$, at a preset signal-to-noise ratio of 0.2. The resulting signal was then expressed as Eq. (1):

$$X(t) = x(t) + w(t). \quad (1)$$

2) EMD was applied to the signal-noise ensemble (the new data series resulting from stacking the original signal onto the white noise), and the resulting IMF components at various levels could then be expressed as Eq. (2):

$$X(t) = \sum_{i=1}^{n} c_i + r_n. \quad (2)$$

3) Steps 1) and 2) were repeated n times, with new white noise of the same amplitude, $w_j(t)$, added to the original signal, $x(t)$, each time. The resulting signal-noise ensemble for the j-th trial could then be expressed as Eq. (3):

$$X_j(t) = \sum_{i=1}^{n} c_{ji} + r_{jn}. \quad (3)$$

4) The IMF component for the jth trial, $c_n(t)$, could then be expressed as Eq. (4):

$$c_n(t) = \frac{1}{n}\sum_{j=1}^{N} c_{j,n}(t). \quad (4)$$

5) The real mode was approximated through multiple averaging operations. The final decomposition result could then be expressed as Eq. (5):

$$x(t) = \sum_{n=1}^{m} c_n(t) + r_m(t). \quad (5)$$

6) A Monte Carlo significance test was then performed on the resultant IMF components, and those with a desired significance level were selected for the subsequent analyses. The energy spectrum density of the kth IMF component could then be expressed as Eq. (6):

$$E_k = \frac{1}{n}\sum_{j=1}^{N} |I_k(j)|^2. \quad (6)$$

where N is the length of an IMF component and $I_k(j)$ is the kth IMF component.

7) The approximate relationship between the mean energy spectrum density, $\overline{E}_k$, and the mean period, $\overline{T}_k$, of the kth IMF component was obtained by performing a Monte Carlo significance test to the white noise as defined by Eq. (7):

$$\ln\overline{E}_k + \ln\left\{\overline{T}_k\right\}_{\mathrm{a}} = 0. \quad (7)$$

Equation (7) is represented as a line with a slope of-1 in a coordinate system with $\left\{\overline{T}_k\right\}_a$ and $\ln\overline{E}_k$ as the horizontal and vertical axes, respectively. Theoretically, the IMF of the white noise falls on the line. However, IMFs obtained during real applications may deviate from the line. Thus, a confidence interval for the energy spectrum distribution of the white noise was defined as Eq. (8):

$$\ln\overline{E}_k = \ln\left\{\overline{T}_k\right\}_{\mathrm{a}} \pm \alpha\sqrt{2/Ne}^{\ln\left(\left\{\overline{T}_k\right\}_{a/2}\right)}, \quad (8)$$

where α is the significance level.

3 Results and discussion

3.1 EEMD and testing of CBP

The EEMD results of the catchment boundary profiles of the 14 samples areas are shown in Table 2. Owing to the self-adaption of EEMD, the decomposition result of each sample area depended entirely on its CBP. Among the 14 sample areas, four (Hengshan, Suide, Jingbian, and Pucheng) had ten IMF components and a residual error term, and ten (Yulin, Jiaxian, Yan'an, Yichuan, Huanglong, Luochuan, Xunyi, Yongshou, and Qianyang) had eleven IMF components and a residual error term. The EEMD results of the 14 samples areas showed that as the decomposition period increased, the frequency gradually decreased. This was because the topography of the Loess Plateau is heterogeneous, nonlinear, and nonstationary. As multiple EEMD trials of IMF components result in an approximation of the real mode, the last term of the decomposition result, the residual error, can be taken as the overall topographic variation trend.

A significance test was performed on the decomposition results for the 14 sample areas. Components with desired significance levels were then used for further investigation of the spatial variation patterns in the topography of the 14 samples areas. To analyze the amount of information with actual physical meaning in the IMF components, the variance contribution rate, period, and confidence level of the components were computed, as shown in Table 2. We note that in order to maintain the total energy of the signal at a desirable level, some IMF components that fell in the area of a significant white noise but failed the significance test were included in the computation of the variance contribution rate.

Figure 3(a) clearly shows that the second IMF component failed the significance test (i.e., it fell below the 95% confidence line), and thus contained relatively less information of actual physical meaning. All of the other IMF components fell above the 99% confidence line and thus contained more information of actual physical meaning. Inspection of Fig. 3(a) and Table 2 reveals that among the IMF components of the CBP from the EEMD for Yulin (excluding the residual, RES), IMF9 had the highest variance contribution rate (2.1906). Thus, the principal period of the catchment boundary topographic relief for Yulin was IMF9. The variation period of IMF9 was then computed and resulted in a mean period of the catchment boundary topographic relief of 1331.25 m for Yulin.

Figure 3(b) and Table 2 show that for the CBP based on the EEMD for Jiaxian, IMF2 and IMF3 failed the

Table 2 Parameters of catchment boundary profiles (CBP) from the ensemble empirical mode decomposition (EEMD) for the 14 sample areas

Sample area	Parameter	IMF1	IMF2	IMF3	IMF4	IMF5	IMF6	IMF7	IMF8	IMF9	IMF10	IMF11	RES
Yulin	Variance contribution rate/%	0.0257	0.0094	0.0063	0.0134	0.1559	0.3753	1.0603	0.8886	2.1906	1.3194	0.0023	93.95
	Period/m	3.2069	6.5619	13.3292	31.1404	69.1558	156.62	287.84	760.71	1331.25	2662.50	2662.50	–
	Confidence level	> 99%	< 95%	> 99%	> 99%	> 99%	> 99%	> 99%	> 99%	> 99%	> 99%	> 99%	–
Jiaxian	Variance contribution rate/%	0.0245	0.0088	0.0053	0.0144	0.1950	0.7115	1.9095	2.4140	1.9461	1.1858	0.0057	91.58
	Period/m	3.2024	6.5572	13.2939	28.1280	64.5175	124.68	307.53	1153.25	1537.67	2306.50	4613	–
	Confidence level	> 99%	< 95%	< 95%	> 99%	> 99%	> 99%	> 99%	> 99%	> 99%	> 99%	> 99%	–
Hengshan	Variance contribution rate/%	0.0215	0.0078	0.0055	0.0252	0.6429	0.7879	1.1816	5.8280	3.7891	0.1401	–	87.57
	Period/m	3.2074	6.3490	13.1131	34.2028	77.3125	140.04	412.33	742.20	1855.50	1855.50	–	–
	Confidence level	> 99%	< 95%	> 99%	> 99%	> 99%	> 99%	> 99%	> 99%	> 99%	> 99%	–	–
Suide	Variance contribution rate/%	0.0218	0.0076	0.0043	0.0096	0.0623	0.1532	0.4667	3.0651	2.6405	2.1114	–	91.46
	Period/m	3.1559	6.4885	13.2582	26.7483	57.5188	131.90	273.21	956.25	1912.50	2550	–	–
	Confidence level	> 99%	< 95%	> 99%	> 99%	> 99%	> 99%	> 99%	> 99%	> 99%	> 99%	–	–
Jingbian	Variance contribution rate/%	0.0303	0.0110	0.0065	0.0175	0.1872	0.3911	2.8338	51.0685	5.9935	0.5473	–	38.91
	Period/m	3.1832	6.5402	13.4409	30.2124	82.2651	126.44	401.65	1707	2276	3414	–	–
	Confidence level	> 99%	< 95%	< 95%	> 99%	> 99%	> 99%	> 99%	> 99%	> 99%	> 99%	–	–
Yan'an	Variance contribution rate/%	0.0257	0.0104	0.0132	0.1480	1.7661	4.2753	5.5753	21.8382	14.5225	1.4284	0.0000	50.40
	Period/m	3.1779	6.5835	14.0599	38.5887	81.7798	185.71	318.36	1114.25	2228.50	4457	Inf	–
	Confidence level	> 99%	< 95%	> 99%	> 99%	> 99%	> 99%	> 99%	> 99%	> 99%	> 99%	> 99%	–
Yichuan	Variance contribution rate/%	0.0212	0.0081	0.0094	0.0319	0.2527	0.6003	0.5286	1.0666	2.0095	0.6038	0.0111	94.86
	Period/m	3.1532	6.5275	14.2943	32.4964	67.9248	148.10	301.13	645.29	1129.25	2258.50	4517	–
	Confidence level	> 99%	< 95%	> 99%	> 99%	> 99%	> 99%	> 99%	> 99%	> 99%	> 99%	> 99%	–
Fuxian	Variance contribution rate/%	0.0228	0.0083	0.0086	0.0618	0.4890	2.3066	3.2257	1.4275	8.2622	0.7899	0.2519	83.15
	Period/m	3.2153	6.6503	13.7288	36.9815	74.2370	169.86	357.93	626.38	1670.33	5011	5011	–
	Confidence level	> 99%	< 95%	> 99%	> 99%	> 99%	> 99%	> 99%	> 99%	> 99%	> 99%	> 99%	–

(*Continued*)

Sample area	Parameter	IMF1	IMF2	IMF3	IMF4	IMF5	IMF6	IMF7	IMF8	IMF9	IMF10	IMF11	RES
Huanglong	Variance contribution rate/%	0.0303	0.0115	0.0154	0.1243	1.2210	6.3551	4.3871	33.7958	24.4366	3.1237	0.0000	26.50
	Period/m	3.1993	6.4540	13.9381	37.3712	83.9020	171.16	534.88	1069.75	2852.67	4279	4279	–
	Confidence level	> 99%	< 95%	> 99%	> 99%	> 99%	> 99%	> 99%	> 99%	> 99%	> 99%	> 99%	–
Luochuan	Variance contribution rate/%	0.0253	0.0090	0.0084	0.0980	0.4167	0.4735	1.0070	0.7850	2.6711	1.6407	0.0002	92.87
	Period/m	3.2607	6.6089	14.1743	34.1984	69.5000	130.58	331.46	538.63	2154.50	4309	Inf	–
	Confidence level	> 99%	< 95%	> 99%	> 99%	> 99%	> 99%	> 99%	> 99%	> 99%	> 99%	> 99%	–
Xunyi	Variance contribution rate/%	0.0228	0.0081	0.0056	0.0180	0.0740	0.1037	0.2634	2.2865	3.3380	0.1924	0.0001	93.69
	Period/m	3.2047	6.4654	13.3469	33.7381	61.1655	130.80	354.25	850.20	2125.50	4251	8502	–
	Confidence level	> 99%	< 95%	> 99%	> 99%	> 99%	> 99%	> 99%	> 99%	> 99%	> 99%	> 99%	–
Pucheng	Variance contribution rate/%	0.0293	0.0117	0.0135	0.0235	0.1500	0.3681	1.0154	1.5289	1.6306	0.9683	–	94.26
	Period/m	3.2175	6.4375	13.4799	27.7034	61.8000	133.90	365.18	1004.25	2008.50	2678	–	–
	Confidence level	> 99%	< 95%	> 99%	> 99%	> 99%	> 99%	> 99%	> 99%	> 99%	> 99%	–	–
Yongshou	Variance contribution rate/%	0.0229	0.0090	0.0077	0.0358	0.7214	2.1104	2.8088	4.2091	2.6032	0.3255	0.0001	87.15
	Period/m	3.1928	6.5444	14.1130	32.8986	87.7297	173.89	347.79	973.80	1623	4869	9738	–
	Confidence level	> 99%	< 95%	> 99%	> 99%	> 99%	> 99%	> 99%	> 99%	> 99%	> 99%	> 99%	–
Qianyang	Variance contribution rate/%	0.0283	0.0103	0.0051	0.0074	0.0681	0.1433	0.5041	4.0998	7.5288	0.8433	0.0041	86.76
	Period/m	3.2012	6.4856	13.2217	27.7538	53.1149	128.36	770.17	924.20	2310.50	3080.67	4621	–
	Confidence level	> 99%	< 95%	< 95%	> 99%	> 99%	> 99%	> 99%	> 99%	> 99%	> 99%	> 99%	–

Note: IMF: intrinsic mode function; RES: residual.

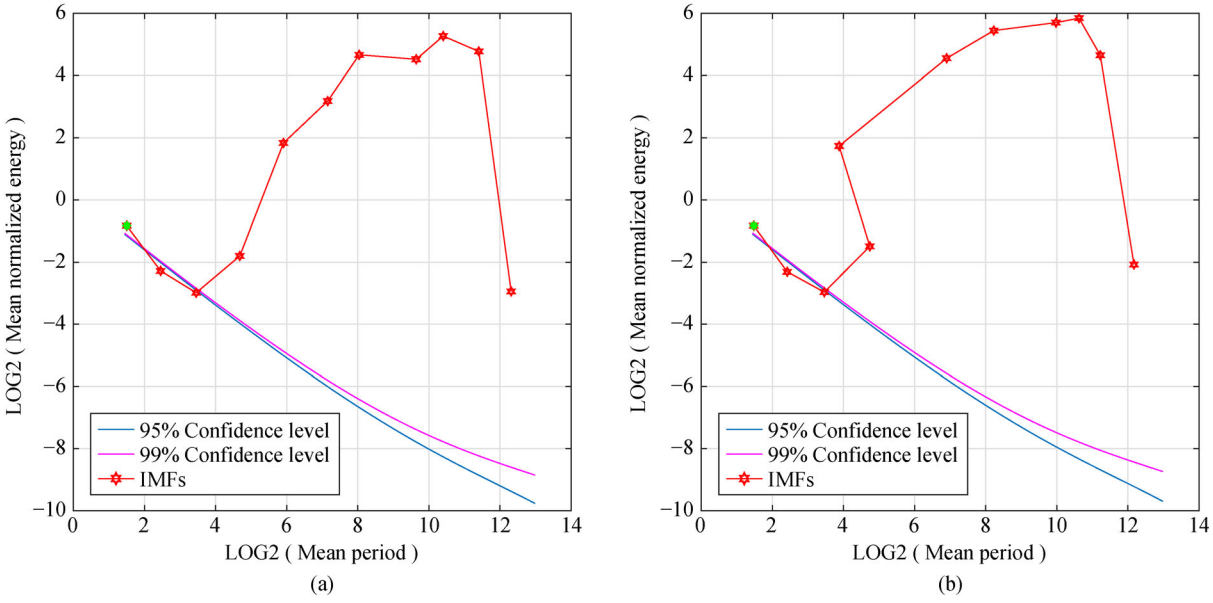

Fig. 3 Significance test for the catchment boundary profiles from the ensemble empirical mode decomposition (EEMD) for (a) Yulin and (b) Jiaxian. IMFs: intrinsic mode functions.

significance test; of the IMF components that passed the significance test (excluding the RES), IMF8 had the highest variance contribution rate (2.4140) and the highest confidence level. Thus, the principal period of the catchment boundary topographic relief for Jiaxian was IMF8. The variation period of IMF8 was then computed and yielded a mean period of the catchment boundary topographic relief of 1153.25 m for Jiaxian.

It can been seen from Fig. 4(a) and Table 2 that among the IMF components of the CBP from the EEMD for Hengshan, IMF2 had a confidence level of $< 95\%$; of all the IMF components with confidence levels $> 99\%$ (excluding the RES), IMF8 had the highest variance contribution rate (5.8280) and was thus most representative of the topographic features of this sample area. Thus, the principal period of the CBP topographic relief for Hengshan was IMF8. The variation period of IMF8 was computed and resulted in a mean period of the catchment boundary topographic relief of 742.20 m for Hengshan.

Figure 4(b) and Table 2 reveal that among the IMF

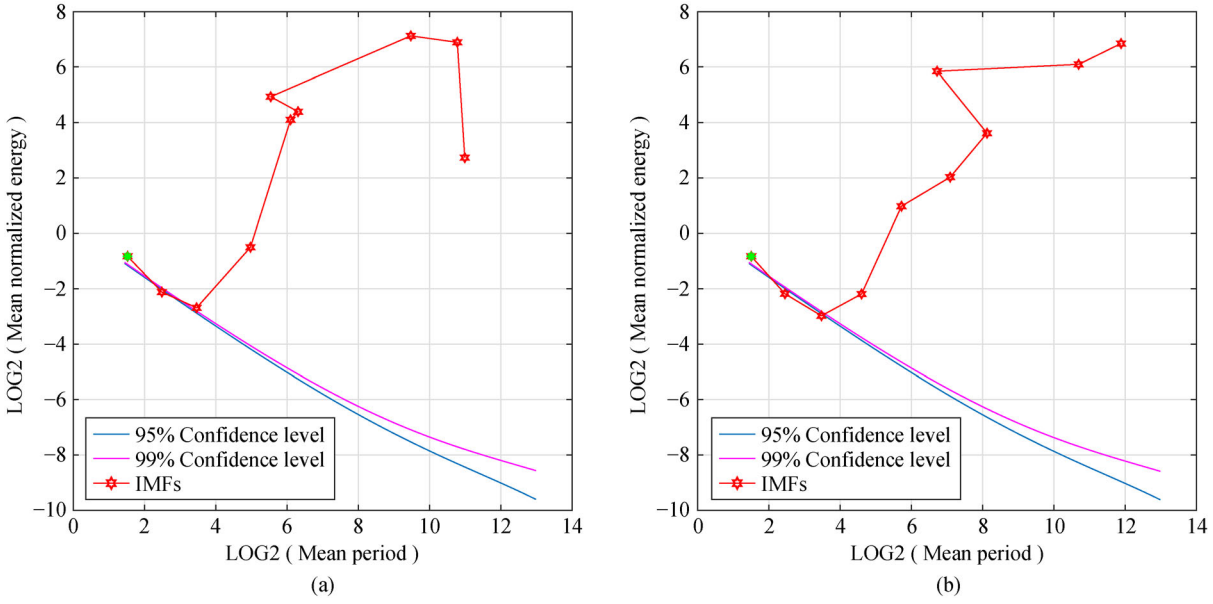

Fig. 4 Significance test for the catchment boundary profiles from the ensemble empirical mode decomposition (EEMD) for (a) Hengshan and (b) Suide. IMFs: intrinsic mode functions.

components of the CBP based on the EEMD for Suide, IMF2 failed the significance test; of the IMF components that passed the significance test (excluding the RES), IMF8 had the highest variance contribution rate (3.0651) and the highest confidence level. Thus, the principal period of the catchment boundary topographic relief for Suide was IMF8. The variation period of IMF8 was computed using the equation for the mean period computation, and yielded a mean period of the CBP topographic relief of 956.25 m for Suide.

It can be seen from Fig. 5(a) and Table 2 that among the ten IMF components of the CBP from the EEMD for Jingbian, IMF2 and IMF 3 fell below the 95% confidence line and failed the significance test, while the other IMF components fell above the 99% confidence line; among the significant IMF components (excluding the RES), IMF8 had the highest variance contribution rate (51.0685). Thus, the principal period of the catchment boundary topographic relief for Jingbian was IMF8. The variation period of IMF8 was computed and yielded a mean period of the catchment boundary topographic relief of 1707 m for Jingbian.

Figure 5(b) and Table 2 show that among the IMF components of the CBP based on the EEMD for Yan'an, IMF2 failed the significance test; of the IMF components that passed the significance test (excluding the RES), IMF8 had the highest variance contribution rate (21.8382). Thus, the principal period of the catchment boundary topographic relief for Yan'an was IMF8. The variation period of IMF8 was computed and resulted in a mean period of the catchment boundary topographic relief of 1114.25 m for Yan'an.

It can be seen from Fig. 6(a) and Table 2 that among the 11 IMF components of the CBP from the EEMD for Yichuan, only IMF2 failed the significance test and thus contained relatively less information of actual physical meaning; of the other IMF components (excluding the RES), IMF9 had the highest variance contribution rate (2.0095). Thus, the principal period of the catchment boundary topographic relief for Yichuan was IMF9. The variation period of IMF9 was computed and yielded a mean period of the catchment boundary topographic relief of 1129.25 m for Yichuan.

Figure 6(b) and Table 2 show that among the IMF components of the CBP based on the EEMD for Fuxian, IMF2 also failed the significance test; of the IMF components that passed the significance test (excluding the RES), IMF9 had the highest variance contribution rate (8.2622). Thus, the principal period of the catchment boundary topographic relief for Fuxian was IMF9. The variation period of IMF9 was computed and resulted in a mean period of the catchment boundary topographic relief of 1670.33 m for Fuxian.

It can be seen from Fig. 7(a) and Table 2 that among the 11 IMF components of the CPB from the EEMD for Huanglong, IMF2 failed the significance test; of all the components that passed the significance test (excluding the RES), IMF8 had the highest variance contribution rate (33.7958). Thus, the principal period of the catchment boundary topographic relief for Huanglong was IMF8. The variation period of IMF8 was computed and yielded a mean period of the catchment boundary topographic relief of 1069.75 m for Huanglong.

Figure 7(b) and Table 2 reveal that among the IMF

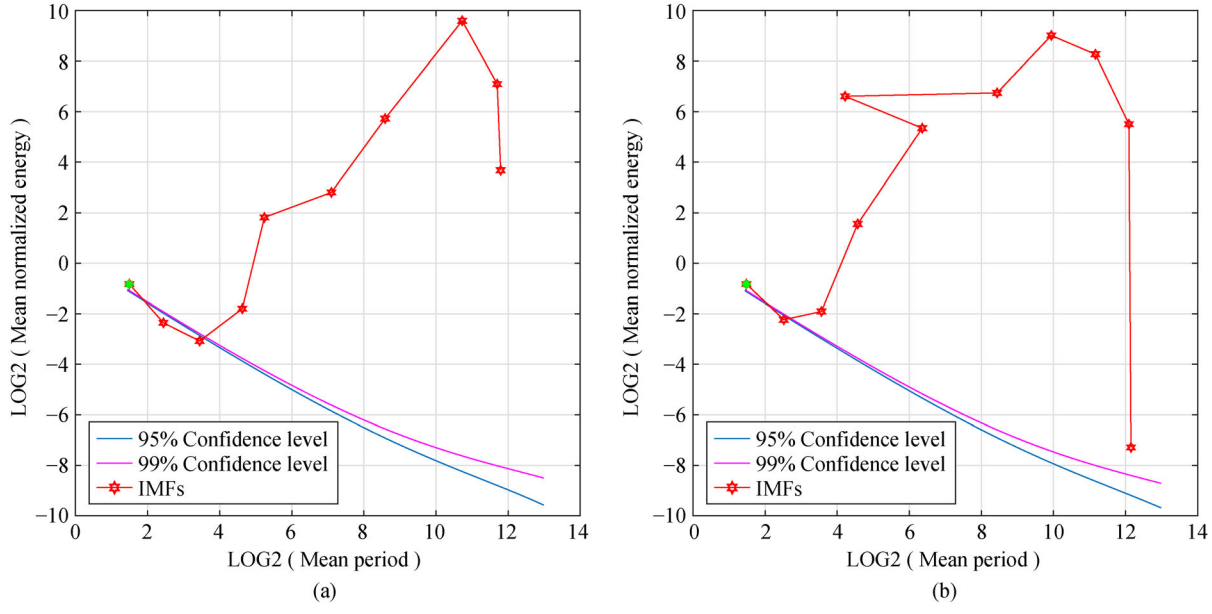

Fig. 5 Significance test for the catchment boundary profiles from the ensemble empirical mode decomposition (EEMD) for (a) Jingbian and (b) Yan'an. IMFs: intrinsic mode functions.

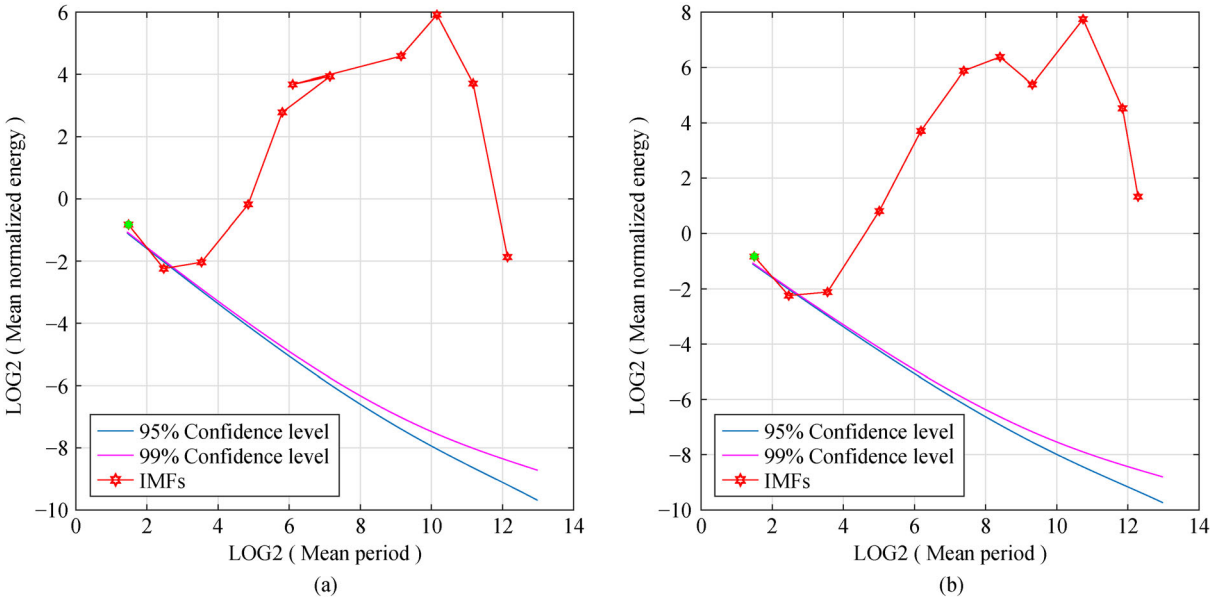

Fig. 6 Significance test for the catchment boundary profiles from the ensemble empirical mode decomposition (EEMD) for (a) Yichuan and (b) Fuxian. IMFs: intrinsic mode functions.

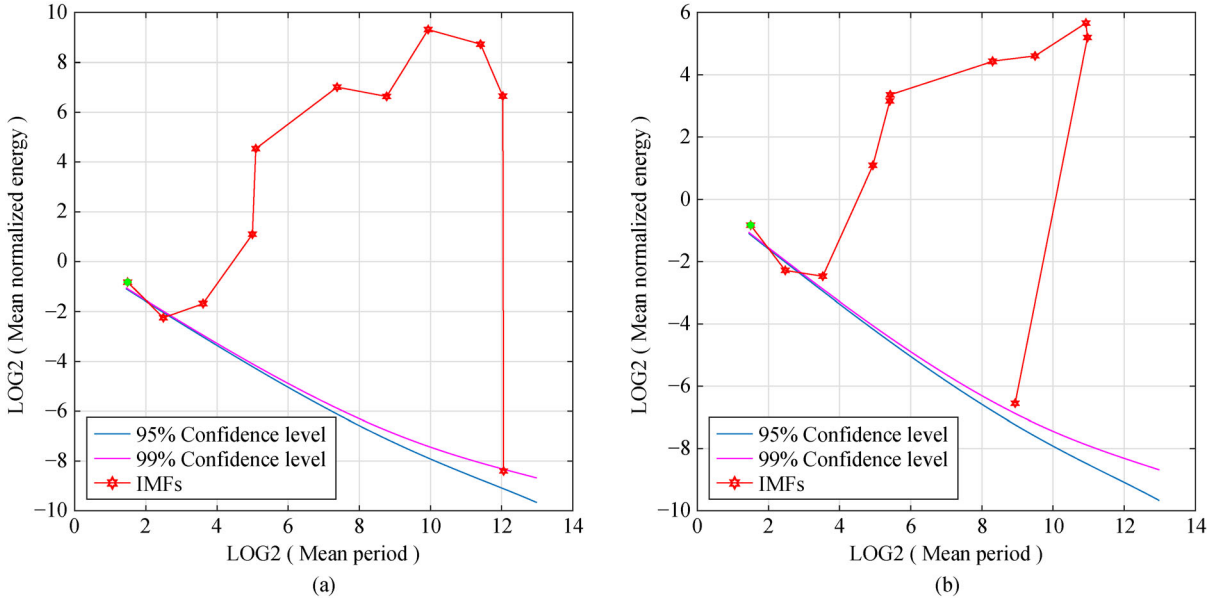

Fig. 7 Significance test for the catchment boundary profiles from the ensemble empirical mode decomposition (EEMD) for (a) Huanglong and (b) Luochuan. IMFs: intrinsic mode functions.

components of the CBP based on the EEMD for Luochuan, IMF2 had a confidence level of $< 95\%$, while the other components had confidence levels $> 99\%$; of all the components with confidence levels $> 99\%$ (excluding the RES), IMF9 had the highest variance contribution rate (2.6711). Thus, the principal period of the catchment boundary topographic relief for Luochuan was IMF9. The variation period of IMF9 was computed and yielded a mean period of the catchment boundary topographic relief of 2154.50 m for Luochuan.

Figure 8(a) and Table 2 show that among the IMF components of the CBP from the EEMD for Xunyi, IMF2 failed the significance test; of the components that passed the significance test (excluding the RES), IMF9 had the highest variance contribution rate (3.3380). Thus, the principal period of the catchment boundary topographic relief for Xunyi was IMF9. The variation period of IMF9 was computed and resulted in a mean period of the catchment boundary topographic relief of 2125.50 m for Xunyi.

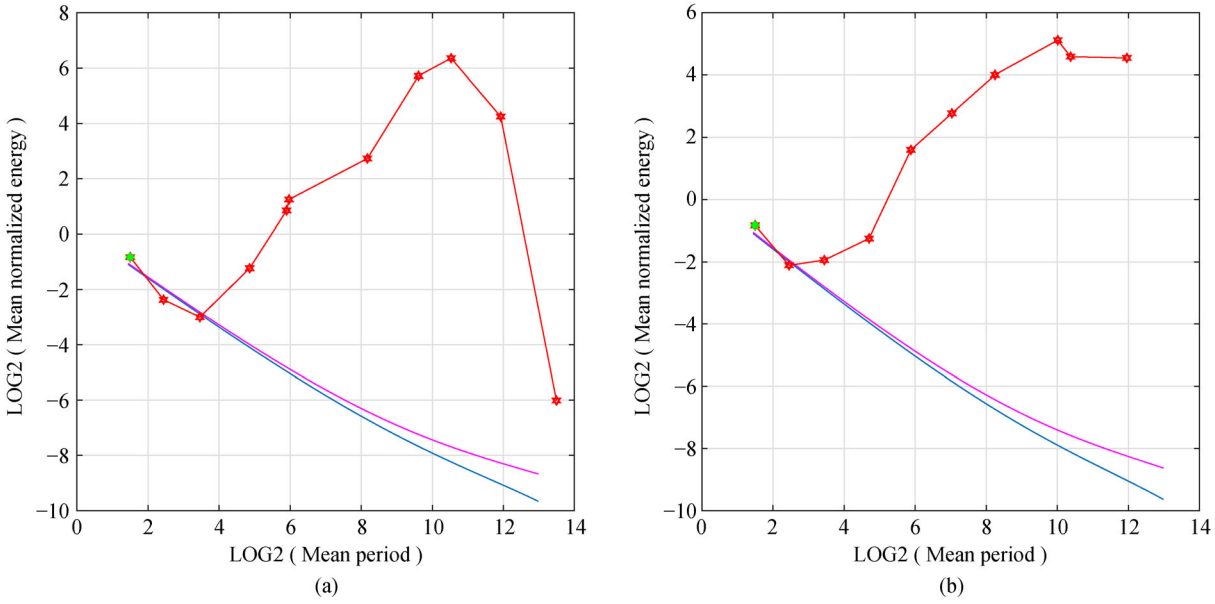

Fig. 8 Significance test for the catchment boundary profiles from the ensemble empirical mode decomposition (EEMD) for (a) Xunyi and (b) Pucheng. IMFs: intrinsic mode functions.

It can be seen from Fig. 8(b) and Table 2 that among the ten IMF components of the CBP based on the EEMD for Pucheng, IMF2 also failed the significance test and thus contained relatively less information of actual physical meaning; of the components that passed the significance test (excluding the RES), IMF9 had the highest variance contribution rate (1.6306). Thus, the principal period of the catchment boundary topographic relief for Pucheng was IMF9. The variation period of IMF9 was computed and yielded a mean period of the catchment boundary topographic relief of 2008.50 m for Pucheng.

Figure 9(a) and Table 2 reveal that among the IMF components of the CBP from the EEMD for Yongshou, IMF2 failed the significance test; of the components that passed the significance test (excluding the RES), IMF8 had the highest variance contribution rate (4.2091). Thus, the principal period of the catchment boundary topographic relief for Yongshou was IMF8. The variation period of

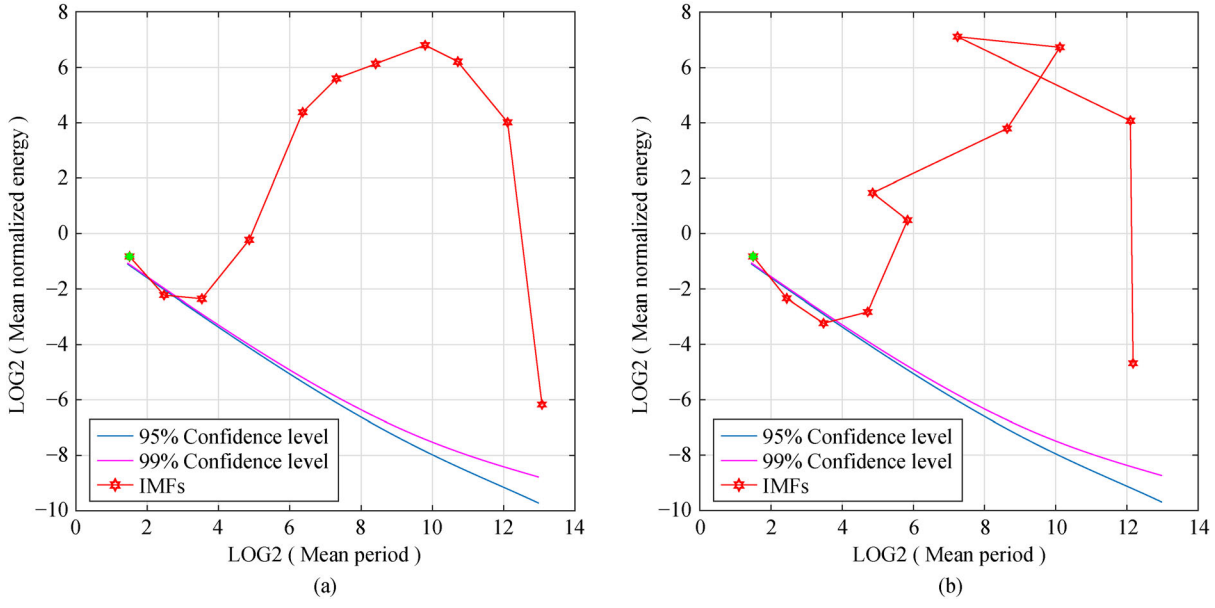

Fig. 9 Significance test for the catchment boundary profiles from the ensemble empirical mode decomposition (EEMD) for (a) Yongshou and (b) Qianyang. IMFs: intrinsic mode functions.

IMF8 was computed and resulted in a mean period of the catchment boundary topographic relief of 973.80 m for Yongshou.

Finally, Fig. 9(b) and Table 2 show that among the IMF components of the CBP based on the EEMD for Qianyang, IMF2 and IMF3 failed the significance test; of the components that passed the significance test (excluding the RES), IMF9 had the highest variance contribution rate (7.5288). Thus, the principal period of the catchment boundary topographic relief for Qianyang was IMF9. The variation period of IMF9 was computed and yielded a mean period of the catchment boundary topographic relief of 2310.50 m for Qianyang.

3.2 CBP topographic relief characteristics

The sequence of the 14 sample sites in terms of topographic relief were ranked from high to low as: Qianyang, Luochuan, Xunyi, Pucheng, Jingbian, Fuxian, Yulin, Jiaxian, Yichuan, Yan'an, Huanglong, Yongshou, Suide, and Hengshan. The major topographic relief characteristics of the Loess Plateau were determined to be in the north–south direction, the period of topographic relief increases, while the spatial frequency of topographic relief decreases. Four sample areas located in loess tablelands of the southern Loess Plateau — Qianyang, Luochuan, Xunyi, and Pucheng — were found to have the lowest spatial frequency of topographic relief. This is because the tablelands have a relatively integrated land surface, with fewer complicated gullies than other areas of the Loess Plateau. Six sample areas — Jingbian, Fuxian, Yulin, Jiaxian, Yichuan, and Yan'an — were determined to have slightly higher spatial frequencies of topographic relief compared with the aforementioned four samples areas. Among these, Yulin and Jiaxian are located in desert-loess transition areas of the northern Loess Plateau, which is characterized by relatively low precipitation, less severe water erosion, and a lower density of gully than other areas of the Loess Plateau. Jingbian, Fuxian, Yichuan, and Yan'an, on the other hand, are located in hill-gully areas of the southern Loess Plateau, which is characterized by relatively a low density of gullies compared with the loess tablelands. The remaining sample areas — Huanglong, Yongshou, Suide, and Hengshan — were found to have the highest spatial frequencies of topographic relief. These four sample areas are located in typical loess hill-gully areas, which have many hills and rugged landforms with significant topographic relief, and are therefore characterized by a low stability of surface matter and a high possibility of gully erosion.

Topographic relief is a geographical field with a strong self-affinity and self-similarity (Bertassello et al., 2018). The topographic relief of different types of loess landforms exhibits great heterogeneity (Li et al., 2015). As an important theory and method of geomorphology (Mark and Aronson, 1984), fractals are of great significance to the development and evolution of surface topography (Czirók et al., 1994), type division (Andrle, 1992), and change simulation and prediction (Cao et al., 2015; Luo et al., 2018). Some parameters of the multifractal spectrum can describe and express the similarities and differences between objects from a local and global perspective (Ariza-Villaverde et al., 2015; Dutta, 2017). For a relatively large width in the multifractal spectrum, the multifractal structure of the CBP data series presented a large global variation. Conversely, for a relatively small multifractal spectrum width, the multifractal structure of the CBP topographic relief data series showed a small global fluctuation. The multifractal spectrum has a long left-tail when the CBP topographic relief data series has a multifractal structure that is sensitive to local fluctuations with large magnitudes (Ihlen, 2012). In contrast, the multifractal spectrum has a long right-tail when the CBP topographic relief data series has a multifractal structure that is sensitive to local fluctuations with small magnitudes (Kantelhardt et al., 2002). Thus, the width and shape of the multifractal spectrum are able to classify a wide range of different scale invariant structures of the CBP topographic relief data series (Kantelhardt et al., 2003; Cao et al., 2017; Cao et al., 2018). It can be seen from Figs. 10(c), 10(f), 10(i), and 10(m) that the multifractal spectrum curve exhibits a distinct left-bias curve with a long right-tail, and that the spectral width of the multifractal spectrum curve is 1.1111. This means that the CBP topographic relief of Hengshan, Yan'an, Huanglong, and Yongshou is dominated by local small fluctuations, and the global variation is mainly based on large fluctuations. In Figs. 10(a), 10(d), 10(g), 10(j), 10(k), and 10(n), the shape of the multifractal spectrum curve exhibits a hook-shaped curve with a long right-tail, and the multifractal spectrum width of these sampling sites are > 1.2192. This indicates that the topographic relief features of the CBP in Yulin, Suide, Yichuan, Luochuan, Xunyi, and Qianyang are characterized by smaller local fluctuations and larger global amplitude fluctuations. In Figs. 10(b), 10(e), and 10(l), the shape of the multifractal spectrum curve reflects an approximate left and right symmetric bell-curve with a larger width (1.2579). This indicates that the topographic relief feature of the CBP in Jiaxian, Jingbian, and Pucheng are characterized by i) local fluctuations that have smaller magnitudes that are intersected by local fluctuations with larger magnitudes, and that they are proportionally the same, and ii) global fluctuations with larger amplitudes. In Fig. 10(h), the shape of the multifractal spectrum curve is also a left-bias curve with a long right-tail, but its multifractal spectrum has the largest width (1.277). This indicates that the topographic relief characteristics of the CBP for the Fuxian sampling sites is also dominated by local fluctuations with small magnitudes, and that the global fluctuations are dominated by the largest amplitudes.

The multifractal form based on the partition function only provides a global description of the data series

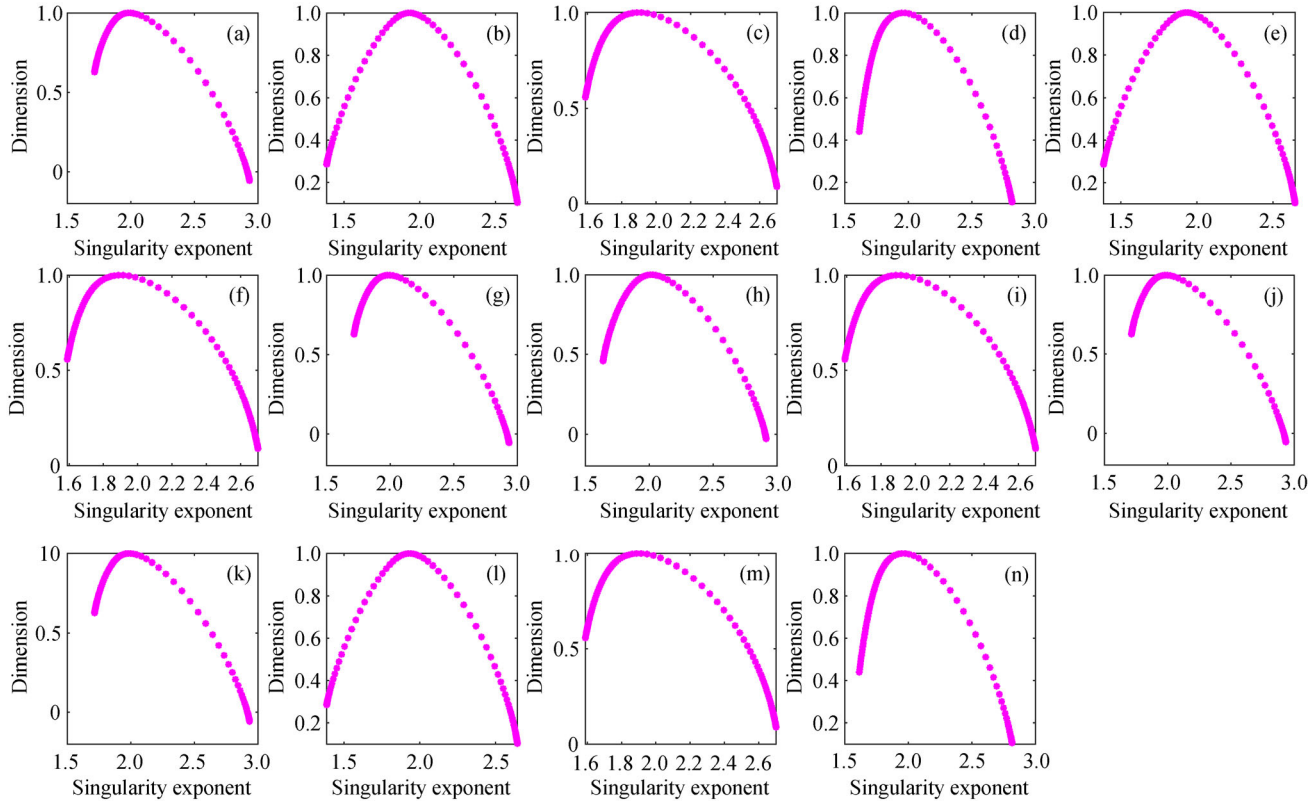

Fig. 10 Multi-fractal spectrum of the catchment boundary profile topographic-relief variation feature of sampling sites on the Loess Plateau, (a)–(n) are Yulin, Jiaxian, Hengshan, Suide, Jingbian, Yan'an, Yichuan, Fuxian, Huanglong, Luochuan, Xunyi, Pucheng, Yongshou, and Qianyang, respectively.

singularity and does not give local information. However, in practical applications, it is often more important to reveal the local singularity information of the data series. The singularity strength and the shape of the multifractal can accurately distinguish the variation characteristics of the data series of study objects from a local and global perspective (Greiner et al., 1998; Struzik, 2000; Stephen and Dixon, 2011; Chhabra and Jensen, 1989). Figure 11 illustrates that according to the singularity strength of the CBP topographic relief variation of different sampling sites, 14 sampling sites could be divided into four types. The singularity strength of sampling sites 3 (Hengshan), 6 (Yan'an), 9 (Huanglong), and 13 (Yongshou) were exactly the same, and belong to a type that involves mainly small fluctuations in the local and global topographic relief. Sampling sites 1 (Yulin), 4 (Suide), 7 (Yichuan), 10 (Luochuan), 11 (Xunyi), and 14 (Qianyang) belong to a type that is characterized by small local fluctuations and large global fluctuations. Sampling sites 2 (Jiaxian), 5 (Jingbian), and 12 (Pucheng) belong to a type that is characterized by both small and large local fluctuations of equal proportions as well as large global fluctuations. Sampling site 8 (Fuxian) was found to be a separate type that is characterized by the smallest local fluctuations and the largest global fluctuations.

4 Conclusions

In this study, the topographic relief of the Loess Plateau was investigated by performing an EEMD of the CBPs of 14 sample areas. A Monte Carlo significance test was performed on the IMF components determined from the EEMD. An in-depth analysis of the variance contribution rate and mean period of the IMF components revealed that components with higher significance levels contained relatively more information of actual physical meaning, and thus better reflect the catchment boundary topographic characteristics. Moreover, this method effectively revealed that areas with higher densities of gullies had smaller TRPs.

The spatial frequency of the topographic relief of the 14 samples areas was then investigated, and revealed that the sequence of the 14 samples areas in terms of topographic relief could be ranked from low to high as: Qianyang (loess tablelands, ridges, and loess-covered medium-elevation hills), Luochuan (medium-relief, high-slope, and medium-elevation hills), Xunyi (medium-altitude loess ridges and tablelands, and low-altitude loess tablelands), Pucheng (loess tablelands, river terraces, and alluvial plains), Jingbian (loess ridges and hills with high shallow gullies), Fuxian (residual loess tablelands), Yulin (wind-deposited

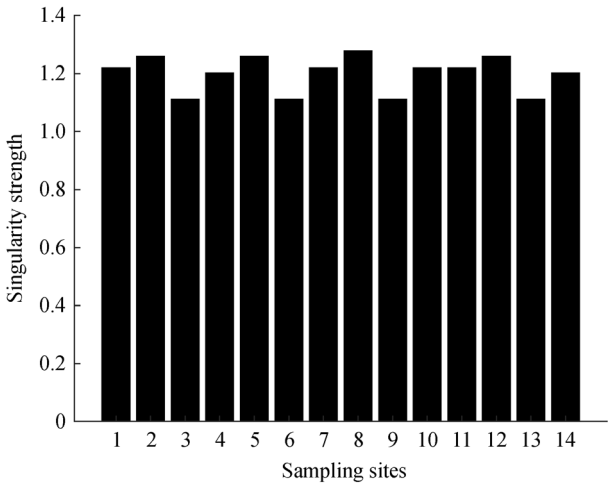

Fig. 11 Singularity strength of the catchment boundary profile topographic-relief variation of sampling sites on the Loess Plateau, where the x-axis represents the sampling sites: 1. Yulin, 2. Jiaxian, 3. Hengshan, 4. Suide, 5. Jingbian, 6. Yan'an, 7. Yichuan, 8. Fuxian, 9. Huanglong, 10. Luochuan, 11. Xunyi, 12. Pucheng, 13. Yongshou, and 14. Qianyang.

sand dunes), Jiaxian (loess hills and ridges with high shallow gullies), Yichuan (loess hills and ridges with high deep gullies), Yan'an (loess-covered, low-slope, and medium-elevation hills), Huanglong (loess tablelands and hills), Yongshou (medium-relief and medium-elevation hills), Suide (loess hills and ridges), and Hengshan (loess hills with high deep gullies).

Of the 14 sample areas, Qianyang was found to have the lowest spatial density of gullies, thus indicating a low topographic relief. Hengshan, followed by Suide, had the highest spatial frequency of gullies, thus indicating a high topographic relief and severe erosion. In comparison with other data analysis methods, the EEMD of the CBPs in combination with the Monte Carlo significance test is more appropriate for investigating the topographic relief characteristics of the Loess Plateau. Through the analysis of the multifractal spectrum and the singularity strength of the fluctuation characteristics of the CBP for the 14 sampling sites, the topographic relief of the Loess Plateau can be divided into four types, the features of which exhibit obvious spatial differences.

Acknowledgements We are grateful for the support of the National Natural Science Foundation of China (Grant Nos. 41930102, 51974314, 41671389 and 41871313). We also thank the professor Guo'an Tang for his significant supervision and the professor Wolfgang Wagner for his critical feedback. We really appreciate the editors and anonymous reviewers for their constructive comments for improving our manuscript.

References

Allen C D (2009). Monitoring environmental impact in the Upper Sonoran Lifestyle: a new tool for rapid ecological assessment. Environ Manage, 43(2): 346–356

Ambreen R, Ahmad I, Qiu X, Li M (2015). Regional and monthly assessment of possible sunshine duration in Pakistan: a geographical approach. J Geogr Inf Syst, 7(01): 65–70

Andrle R (1992). Estimating fractal dimension with the divider method in geomorphology. Geomorphology, 5(1-2): 131–141

Ariza-Villaverde A B, Jiménez-Hornero F J, Gutiérrez de Ravé E (2015). Influence of DEM resolution on drainage network extraction: a multifractal analysis. Geomorphology, 241: 243–254

Badgley C, Smiley T M, Terry R, Davis E B, DeSantis L R G, Fox D L, Hopkins S S B, Jezkova T, Matocq M D, Matzke N, McGuire J L, Mulch A, Riddle B R, Roth V L, Samuels J X, Strömberg C A E, Yanites B J (2017). Biodiversity and topographic complexity: modern and geohistorical perspectives. Trends Ecol Evol, 32(3): 211–226

Bertassello L E, Rao P S C, Botter G, Aubeneau A F (2018). Topographic analysis of wetlandscapes: fractal dimension and scaling properties. EPiC Series in Engineering, 3: 217–226

Bi L, He H, Wei Z, Shi F (2012). Fractal properties of landforms in the Ordos Block and surrounding areas, China. Geomorphology, 175: 151–162

Black B A, Perron J T, Hemingway D, Bailey E, Nimmo F, Zebker H (2017). Global drainage patterns and the origins of topographic relief on Earth, Mars, and Titan. Science, 356(6339): 727–731

Bollati I, Pellegrini M, Reynard E, Pelfini M (2017). Water driven processes and landforms evolution rates in mountain geomorphosites: examples from Swiss Alps. Catena, 158: 321–339

Bumbak S, Ilies M (2014). Implications of relief configuration in the socioeconomic system: the case of Mara Basin, Maramures Land, Romania. Journal of Settlements and Spatial Planning, 3: 31

Cao J, Tang G, Fang X, Li J, Liu Y, Zhang Y, Zhu Y, Li F (2017). Topographic spatial variation analysis of loess shoulder lines in the Loess Plateau of China based on MF-DFA. ISPRS Int J Geoinf, 6(5): 141

Cao J, Tang G, Fang X, Li J, Liu Y, Zhang Y, Li F (2019). Terrain relief periods of loess landforms based on terrain profiles of the Loess Plateau in northern Shaanxi Province, China. Front Earth Sci, 13(2): 410–421

Cao G, He L Y, Cao J (2018). Multifractal detrended fluctuation analysis (mf-dfa). In: Multifractal Detrended Analysis Method and Its Application in Financial Markets. Singapore: Springer

Cao W, Cai Z, Tang Z (2015). Fractal structure of lunar topography: An interpretation of topographic characteristics. Geomorphology, 238: 112–118

Chhabra A, Jensen R V (1989). Direct determination of the f(α) singularity spectrum. Phys Rev Lett, 62(12): 1327–1330

Clarke K C, Romero B E (2017). On the topology of topography: a review. Cartogr Geogr Inf Sci, 44(3): 271–282

Collier P, Forrest D, Pearson A (2003). The representation of topographic information on maps: the depiction of relief. Cartogr J, 40(1): 17–26

Cowley G S, Niemann J D, Green T R, Seyfried M S, Jones A S, Grazaitis P J (2017). Impacts of precipitation and potential evapotranspiration patterns on downscaling soil moisture in regions with large topographic relief. Water Resour Res, 53(2): 1553–1574

Czirók A, Somfai E, Vicsek T (1994). Self-affine roughening in a model

experiment on erosion in geomorphology. Physica A, 205(1-3): 355–366

de Matos-Machado R, Toumazet J P, Bergès J C, Amat J P, Arnaud-Fassetta G, Bétard F, Bilodeau C, Hupy J P, Jacquemot S (2019). War landform mapping and classification on the Verdun battlefield (France) using airborne LiDAR and multivariate analysis. Earth Surf Process Landf, 44(7): 1430–1448

Diefenderfer H L, Sinks I A, Zimmerman S A, Cullinan V I, Borde A B (2018). Designing topographic heterogeneity for tidal wetland restoration. Ecol Eng, 123: 212–225

Dutta S (2017). Decoding the morphological differences between Himalayan Glacial and fluvial landscapes using multifractal analysis. Sci Rep, 7(1): 11032

Dymond S F, Bradford J B, Bolstad P V, Kolka R K, Sebestyen S D, DeSutter T M (2017). Topographic, edaphic, and vegetative controls on plant—available water. Ecohydrology, 10(8): e1897

Farkas C, Kværnø S H, Engebretsen A, Barneveld R, Deelstra J (2016). Applying profile-and catchment-based mathematical models for evaluating the run-off from a Nordic catchment. J Hydrol Hydromech, 64(3): 218–225

Gailleton B, Mudd S M, Clubb F J, Peifer D, Hurst M D (2019). A segmentation approach for the reproducible extraction and quantification of knickpoints from river long profiles. Earth Surface Dynamics, 7(1): 211–230

Gomez B (1984). Typology of segregated (armoured/paved) surfaces: some comments. Earth Surf Process Landf, 9(1): 19–24

Greiner M, Schmiegel J, Eickemeyer F, Lipa P, Eggers H C (1998). Spatial correlations of singularity strengths in multifractal branching processes. Phys Rev E Stat Phys Plasmas Fluids Relat Interdiscip Topics, 58(1): 554–564

Gruber F E, Baruck J, Mair V, Geitner C (2019). From geological to soil parent material maps—a random forest-supported analysis of geological map units and topography to support soil survey in South Tyrol. Geoderma, 354: 113884

Gu Y, Wylie B K (2016). Using satellite vegetation and compound topographic indices to map highly erodible cropland buffers for cellulosic biofuel crop developments in eastern Nebraska, USA. Ecol Indic, 60: 64–70

Hui Y, Yong L, Shaoquan L, Yong W, Yong Y, Weidong L (2015). The influences of topographic relief on spatial distribution of mountain settlements in Three Gorges Area. Environ Earth Sci, 74(5): 4335–4344

Ihlen E A F E (2012). Introduction to multifractal detrended fluctuation analysis in matlab. Front Physiol, 3: 141

Iverson R M, George D L, Allstadt K, Reid M E, Collins B D, Vallance J W, Schilling S P, Godt J W, Cannon C M, Magirl C S, Baum R L, Coe J A, Schulz W H, Bower J B (2015). Landslide mobility and hazards: implications of the 2014 Oso disaster. Earth Planet Sci Lett, 412: 197–208

Kantelhardt J W, Rybski D, Zschiegner S A, Braun P, Koscielny-Bunde E, Livina V, Havlin S, Bunde A (2003). Multifractality of river runoff and precipitation: comparison of fluctuation analysis and wavelet methods. Physica A, 330(1–2): 240–245

Kantelhardt J W, Zschiegner S A, Koscielny-Bunde E, Havlin S, Bunde A, Stanley H E (2002). Multifractal detrended fluctuation analysis of nonstationary time series. Physica A, 316(1–4): 87–114

Karim F, Petheram C, Marvanek S, Ticehurst C, Wallace J, Hasan M (2016). Impact of climate change on floodplain inundation and hydrological connectivity between wetlands and rivers in a tropical river catchment. Hydrol Processes, 30(10): 1574–1593

Khan U, Tuteja N K, Sharma A, Lucas S, Murphy B, Jenkins B (2016). Applicability of Hydrologic Response Units in low topographic relief catchments and evaluation using high resolution aerial photograph analysis. Environ Model Softw, 81: 56–71

Latrubesse E M, Baker P A, Argollo J (2009). Geomorphology of natural hazards and human-induced disasters in Bolivia. Developments in Earth Surface Processes, 13: 181–194

Leger M (1990). Loess landforms. Quat Int, 7: 53–61

Li X, McCarty G W, Karlen D L, Cambardella C A (2018). Topographic metric predictions of soil redistribution and organic carbon in Iowa cropland fields. Catena, 160: 222–232

Li M, Yang X, Na J, Liu K, Jia Y, Xiong L (2017). Regional topographic classification in the north Shaanxi Loess Plateau based on catchment boundary profiles. Prog Phys Geogr, 41(3): 302–324

Li Y (2015). Effects of analytical window and resolution on topographic relief derived using digital elevation models. GIsci Remote Sens, 52 (4): 462–477

Li Y, Zhang T, Zhang Y, Xu Q (2018). Geometrical appearance and spatial arrangement of structural blocks of the Malan loess in NW China: implications for the formation of loess columns. J Asian Earth Sci, 158: 18–28

Liu Y, Deng W, Song X Q (2015). Relief degree of land surface and population distribution of mountainous areas in China. J Mt Sci, 12 (2): 518–532

Li Z W, Zhang G H, Geng R, Wang H (2015). Spatial heterogeneity of soil detachment capacity by overland flow at a hillslope with ephemeral gullies on the Loess Plateau. Geomorphology, 248: 264–272

Luo J, Zheng Z, Li T, He S (2018). Assessing the impacts of microtopography on soil erosion under simulated rainfall, using a multifractal approach. Hydrol Processes, 32(16): 2543–2556

Machowski R, Rzetala M A, Rzetala M, Solarski M (2016). Geomorphological and hydrological effects of subsidence and land use change in industrial and urban areas. Land Degrad Dev, 27(7): 1740–1752

Mackay D S, Band L E (1998). Extraction and representation of nested catchment areas from digital elevation models in lake—dominated topography. Water Resour Res, 34(4): 897–901

MacMillan R A, Shary P A (2009). Landforms and landform elements in geomorphometry. Developments in soil science, 33: 227–254

Mark D M, Aronson P B (1984). Scale-dependent fractal dimensions of topographic surfaces: an empirical investigation, with applications in geomorphology and computer mapping. J Int Assoc Math Geol, 16 (7): 671–683

Marston B E, Jenny B (2015). Improving the representation of major landforms in analytical relief shading. Int J Geogr Inf Sci, 29(7): 1144–1165

Martel S J (2016). Effects of small-amplitude periodic topography on combined stresses due to gravity and tectonics. Int J Rock Mech Min Sci, 89: 1–13

Meng X, Xiong L Y, Yang X W, Yang B S, Tang G A (2018). A terrain

openness index for the extraction of karst Fenglin and Fengcong landform units from DEMs. J Mt Sci, 15(4): 752–764

Na J, Yang X, Dai W, Li M, Xiong L, Zhu R, Tang G (2018). Bidirectional DEM relief shading method for extraction of gully shoulder line in loess tableland area. Phys Geogr, 39(4): 368–386

Nunalee C G, Horváth Á, Basu S (2015). High-resolution numerical modeling of mesoscale island wakes and sensitivity to static topographic relief data. Geosci Model Dev, 8(8): 2645–2653

Orengo H A, Petrie C A (2018). Multi-scale relief model (MSRM): a new algorithm for the visualization of subtle topographic change of variable size in digital elevation models. Earth Surf Process Landf, 43 (6): 1361–1369

Orr H G, Large A R G, Newson M D, Walsh C L (2008). A predictive typology for characterising hydromorphology. Geomorphology, 100 (1–2): 32–40

Persendt F C, Gomez C (2016). Assessment of drainage network extractions in a low-relief area of the Cuvelai Basin (Namibia) from multiple sources: LiDAR, topographic maps, and digital aerial orthophotographs. Geomorphology, 260: 32–50

Robl J, Hergarten S, Prasicek G (2017). The topographic state of fluvially conditioned mountain ranges. Earth Sci Rev, 168: 190–217

Savvides A, Michael A, Malaktou E, Philokyprou M (2016). Examination and assessment of insolation conditions of streetscapes of traditional settlements in the Eastern Mediterranean area. Habitat Int, 53: 442–452

Serrano E, Oliva M, González-García M, López-Moreno J I, González-Trueba J, Martín-Moreno R, Gómez-Lende M, Martín-Díaz J, Nofre J, Palma P (2018). Post-little ice age paraglacial processes and landforms in the high Iberian mountains: a review. Land Degrad Dev, 29(11): 4186–4208

Stephen D G, Dixon J A (2011). Strong anticipation: Multifractal cascade dynamics modulate scaling in synchronization behaviors. Chaos Solitons Fractals, 44(1–3): 160–168

Struzik Z R (2000). Determining local singularity strengths and their spectra with the wavelet transform. Fractals, 8(02): 163–179

Tammelin M, Kauppila T (2018). Quaternary landforms and basin morphology control the natural eutrophy of boreal lakes and their sensitivity to anthropogenic forcing. Front Ecol Evol, 6(65): 1–18

Telbisz T, Bottlik Z, Mari L, Kőszegi M (2014). The impact of topography on social factors: a case study of Montenegro. J Mt Sci, 11(1): 131–141

Wang D, Fu B, Lu K, Xiao L, Zhang Y, Feng X (2010). Multifractal analysis of land use pattern in space and time: a case study in the Loess Plateau of China. Ecol Complex, 7(4): 487–493

Wang Y, Ding Q, Zhuang D (2015). An eco-city evaluation method based on spatial analysis technology: A case study of Jiangsu Province, China. Ecol Indic, 58: 37–46

Wu Z, Huang N E (2009). Ensemble empirical mode decomposition: a noise-assisted data analysis method. Adv Adapt Data Anal, 1(01): 1–41

Wyrick J R, Senter A E, Pasternack G B (2014). Revealing the natural complexity of fluvial morphology through 2D hydrodynamic delineation of river landforms. Geomorphology, 210: 14–22

Xi C B, Qian T L, Chi Y, Chen J, Wang J C (2018). Relationship between settlements and topographical factors: an example from Sichuan Province, China. J Mt Sci, 15(9): 2043–2054

Xiong L Y, Tang G A, Strobl J, Zhu A X (2016). Paleotopographic controls on loess deposition in the Loess Plateau of China. Earth Surf Process Landf, 41(9): 1155–1168

Xiong L Y, Tang G A, Zhu A X, Qian Y Q (2017). A peak-cluster assessment method for the identification of upland planation surfaces. Int J Geogr Inf Sci, 31(2): 387–404

Yang F, Zhou Y (2017). Quantifying spatial scale of positive and negative terrains pattern at watershed-scale: case in soil and water conservation region on Loess Plateau. J Mt Sci, 14(8): 1642–1654

Yang X, Tang G, Meng X, Xiong L (2019). Classification of Karst fenglin and fengcong landform units based on spatial relations of terrain feature points from DEMs. Remote Sens, 11(16): 1950

Zhang J, Zhu W, Zhu L, Cui Y, He S, Ren H (2019). Topographical relief characteristics and its impact on population and economy: a case study of the mountainous area in western Henan, China. J Geogr Sci, 29(4): 598–612

Zhang Y, Fan G, He Y, Cao L (2017). Risk assessment of typhoon disaster for the Yangtze River Delta of China. Geomatics Nat Hazards Risk, 8(2): 1580–1591

Zhao S, Yu Y, Qin D, Yin D, Du Z, Li J, Dong L, He J, Li P (2019). Measurements of submicron particles vertical profiles by means of topographic relief in a typical valley city, China. Atmos Environ, 199: 102–113

Zhou L, Xiong L Y (2018). Natural topographic controls on the spatial distribution of poverty-stricken counties in China. Appl Geogr, 90: 282–292

Zhou Y, Tang G A, Yang X, Xiao C, Zhang Y, Luo M (2010). Positive and negative terrains on northern Shaanxi Loess Plateau. J Geogr Sci, 20(1): 64–76